Large eddy simulations of a circular orifice jet with and without a cross-sectional exit plate

2014 Chinese Phys. B 23 044704

(http://iopscience.iop.org/1674-1056/23/4/044704)

Large eddy simulations of a circular orifice jet with and without a cross-sectional exit plate*

Zhang Jian-Peng(张健鹏)[a], Xu Min-Yi(徐敏义)[b], and Mi Jian-Chun(米建春)[a,c]†

[a] State Key Laboratory of Turbulence & Complex Systems, College of Engineering, Peking University, Beijing 100871, China
[b] Marine Engineering College, Dalian Maritime University, Dalian 116026, China
[c] College of Energy & Power Engineering, Changsha University of Science and Technology, Changsha 410004, China

(Received 7 June 2013; revised manuscript received 27 September 2013; published online 20 February 2014)

The effect of a cross-sectional exit plane on the downstream mixing characteristics of a circular turbulent jet is investigated using large eddy simulation (LES). The turbulent jet is issued from an orifice-type nozzle at an exit Reynolds number of 5×10^4. Both instantaneous and statistical velocity fields of the jet are provided. Results show that the rates of the mean velocity decay and jet spread are both higher in the case with the exit plate than without it. The existence of the plate is found to increase the downstream entrainment rate by about 10% on average over the axial range of 8–30d_e (exit diameter). Also, the presence of the plate enables the formation of vortex rings to occur further downstream by 0.5–1.0d_e. A physical insight into the near-field jet is provided to explain the importance of the boundary conditions in the evolution of a turbulent jet. In addition, a method of using the decay of the centreline velocity and the half-width of the jet to calculate the entrainment rate is proposed.

Keywords: circular orifice jet, large eddy simulation (LES), exit plate, entrainment

PACS: 47.27.ep, 47.27.wg, 47.85.lk **DOI:** 10.1088/1674-1056/23/4/044704

1. Introduction

Circular turbulent jets have been extensively investigated, owing to their important role in fundamental research on turbulence and wide applications in industries, and also our daily life. Typically three types of circular nozzles are commonly used: long pipe (LP), smooth contraction (SC), and orifice plate (OP). A great number of experimental and theoretical studies have focused on the velocity and scalar mixing characteristics of circular free jets, in both mean and instantaneous terms, from LP and particularly SC.[1–8] Numerical studies of circular jets[9–12] often use LP or SC nozzles due to the above-mentioned reason, which may be regarded as one key reason, in addition to the simplicity in realizing and adjusting the inlet profiles of both LP (often 1/7-power law) and SC ('top-hat') jets.

Relatively speaking, the OP jet has drawn little attention for fundamental study on jets, perhaps due to its very complex flow structure around the exit plate, resulting in complicated initial velocity profiles. Mi *et al.*[13] have reported on some properties of the OP jet by comparing the jets issuing from nine differently shaped nozzles. The mixing characteristics of the OP jet were explored by Mi *et al.*[14] using flow visualizations and temperature measurements. They found that the OP jet has the greatest entrainment with the ambient fluid since the structures in the initial region of the OP jet are more three-dimensional. Quinn[15] used hotwire (HW) velocimetry to investigate the velocity properties of the OP jet and discovered that the centerline mean velocity decays faster for the OP jet than for the SC jet. Other properties like mean streamwise velocity, the turbulent Reynolds stress, and the autocorrelation coefficients of the OP jet were also reported. Recently Mi *et al.*[16] used particle image velocimetry (PIV) techniques to unveil more properties including the instant flow field of the OP jet of high Reynolds number and confirmed the phenomenon reported by Quinn. Previous studies have shown that the evolution of the jet is strongly related to the near-field three-dimensional motions.[17–19] Yet, the vortical structures of the OP jet remain unknown while the vortical structures of SC and LP jets have been investigated by flow visualization techniques and numerical simulations. The numerical simulation is a good way to reveal the three-dimensional motions and other profiles of the OP jet. Unfortunately, no such work has been conducted, perhaps due to the nozzle exit conditions being more complicated than those of LP and SC jets.

The exit profiles are of great importance for the downstream development of the jet, so, numerous studies have focused on this topic.[4,7,10,12,20–23] Nevertheless, the environmental condition of the exit, which also influences the evolution of the jet, has been less concerned. Babu and Mahesh[24] and Romano[25] have investigated the effects of the cross-sectional exit plate (Fig. 1) using direct numerical simulation (DNS) and flow visualization techniques, respectively. While the DNS results of an LP jet by Babu and Mahesh showed that

*Project supported by the National Natural Science Foundation of China (Grant Nos. 11072005 and 10921202) and the Fundamental Research Funds for the Central Universities, China (Grant No. 3132013029).

†Corresponding author. E-mail: jcmi@coe.pku.edu.cn

the exit plate has minor effects on the jet profiles, the experimental results of an SC jet by Romano manifested that the evolution of the vortical structures is significantly affected by the exit plate, even the statistical profiles of the SC jet have some differences. To the best of our knowledge, the effects of an exit plate on the OP jet have not been studied yet. The opposite results presented by Babu and Mahesh[24] and Romano[25] imply the necessity of the investigation on how the exit plate influences the development of an OP jet.

The present study is to address the deficits indicated above. The main objectives are (i) to provide flow field data of the OP jet using numerical simulation and (ii) to examine the influence of the cross-sectional exit plane on the downstream flow of an OP jet by using both the instantaneous and statistical properties of the flow and thus providing physical insight into the jet. Also, the investigation on the exit-plate effect will benefit the jet applications in industry. To this end, computations by large eddy simulation (LES) based on the dynamic Smagorinsky–Lilly subgrid-scale model of the OP jets in the cases with and without the exit plate are performed at $R_e = 5\times10^4$, where $R_e = U_j d_e/\nu$, with U_j being the bulk mean velocity of the exit, d_e the exit diameter and ν the fluid kinematic viscosity.

2. Computational details

2.1. Governing equations and numerical methods

The filtered governing equations of viscous incompressible flow for LES are

$$\frac{\partial \overline{u_i}}{\partial t} + u_j \frac{\partial \overline{u_i u_j}}{\partial x_j} = -\frac{1}{\rho}\frac{\partial \overline{p}}{\partial x_i} + \nu \frac{\partial^2 \overline{u_i}}{\partial x_j} - \frac{\partial\left(\overline{u_i u_j} - \overline{u_i}\,\overline{u_j}\right)}{\partial x_j}, \tag{1}$$

$$\frac{\partial \overline{u_i}}{\partial x_i} = 0, \tag{2}$$

where x_i ($i = 1, 2, 3$) are the coordinates, are the filtered velocity components, $\overline{p}$ is the filtered pressure, ρ and ν are the density and kinematic viscosity of the fluid respectively, which are both considered to be constant. The subgrid-scale (SGS) stress tensor

$$\tau_{ij} = \overline{u_i u_j} - \overline{u_i}\,\overline{u_j} \tag{3}$$

is modeled by Smagorinsky as

$$\tau_{ij} - \frac{1}{3}\delta_{ij}\tau_{kk} = -2\nu_t \overline{S_{ij}}, \tag{4}$$

where δ_{ij} is Kronecker's delta, ν_t is the Smagorinsky eddy viscosity, and is the resolved strain rate tensor, which is defined as

$$\overline{S}_{ij} = \frac{1}{2}\left(\frac{\partial \overline{u_i}}{\partial x_j} + \frac{\partial \overline{u_j}}{\partial x_i}\right). \tag{5}$$

For the original Smagorinsky SGS model, the Smagorinsky eddy viscosity is estimated by

$$\nu_t = L_s^2 \left|\overline{S}\right| \tag{6}$$

with and L_s being the mixing length for subgrid scales computed as

$$L_s = \min(\kappa d, C_s \Delta), \tag{7}$$

with κ being the von Kármán constant, d the distance to the closest wall, C_s the Smagorinsky constant, and $\Delta = V^{1/3}$ the local grid scale for filtering (here V is the computational cell volume). In the dynamic Smagorinsky–Lilly model, which was proposed by Germano *et al.*[26] and subsequently modified by Lilly,[27] a second, coarser spatial filter (called the test filter) is applied. At the second filter, the stress tensor can be expressed as

$$T_{ij} = \widehat{\overline{u_i u_j}} - \widehat{\overline{u}_i}\,\widehat{\overline{u}_j}, \tag{8}$$

where the hat symbol $\widehat{\ }$ denotes the second filter.

By applying the Smagorinsky SGS model, the sub-test scale stress tensor can be similarly approximated by

$$T_{ij} - \frac{1}{3}\widehat{\sigma} T_{kk} = -2C\widehat{\Delta}\left|\widehat{\overline{S}}\right|\widehat{\overline{S}}_{ij}, \tag{9}$$

where $\hat{\Delta} = 2\Delta$ is the test filter scale, and C is the Smagorinsky constant (square of the original quantity). Germano *et al.*[26] related the sub-grid scale stress to the sub-test scale stress by

$$L_{ij} = T_{ij} - \hat{\tau}_{ij} = \widehat{\overline{u}_i}\,\widehat{\overline{u}_j} - \widehat{\overline{u}_i}\,\widehat{\overline{u}_j}, \tag{10}$$

where L_{ij} can be computed explicitly from the resolved scale stress.

Subtracting a second filtered result of Eq. (4) from Eq. (9) and using Eq. (10), one has the relationship between L_{ij} and the Smagorinsky constant C. Using the least-square method to solve C and noting that in an incompressible flow, we have

$$C = \frac{1}{2}\frac{L_{ij}M_{ij}}{M_{ij}^2}, \tag{11}$$

where

$$M_{ij} = \Delta^2 \widehat{\left|\overline{S}\right|\overline{S}_{ij}} - \widehat{\Delta}^2 \left|\widehat{\overline{S}}\right|\widehat{\overline{S}}_{ij}. \tag{12}$$

From the above equation, it can be seen that C is a local value varying both with time and space in the dynamic Smagorinsky–Lilly model. To avoid numerical divergence, C is clipped in a range from 0 to 0.23 in the present simulation. The equations of the dynamic Smagorinsky–Lilly LES model are solved by a finite volume method based on FLUENT v6.3 with the boundary conditions implemented through the user-defined function (UDF) feature, which are to be discussed in the following section. For temporal discretization, a second-order implicit scheme is used and a bounded central difference scheme is used for spatial discretization. The PISO method is applied to the pressure-velocity coupling.

2.2. Physical model and the grid

The nozzle configuration for present simulation is shown in Fig. 1, which is similar to that in Mi *et al.*'s[16] experiment. The nozzle is characterized by an air supply tube with 25.4 mm in diameter, i.e., $D = 25.4$ mm (1.0 inch), and an orifice plate serving as the outlet with an exit diameter of $d_e = 12.5$ mm. Two cases for the present study are considered, i.e., a jet issuing from the nozzle exit (a) with and (b) without a flat plate of 278.4 mm in diameter. The bulk mean velocity of incompressible air issuing from both nozzles is $U_j = 58.71$ m/s at room temperature, which produces the corresponding Reynolds number $Re = 5 \times 10^4$.

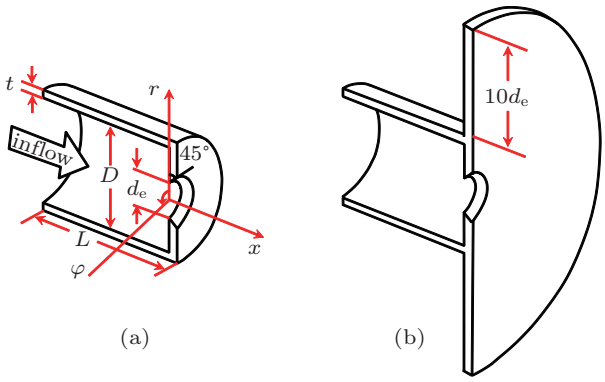

Fig. 1. (color online) Schematic diagrams of the nozzle with $d_e = 12.5$ mm, $D = 25.4$ mm (1.0 inch), $L = 62.5$ mm, and $t = 1.5$ mm in the cases (a) without exit plate and (b) with exit plate.

According to the coordinates and the scales specified in Fig. 1(a), the size of the computational domain is $-5 < x/d_e < 30$ for the axial range, $r/d_e \leq 11$ for the radial range and $0 \leq \varphi \leq 2\pi$ for the azimuthal range, respectively. By doubling the domain radius, it is found that the domain radius of $11d_e$ is sufficiently large for the present simulations of the mean and fluctuating flow fields. A similar domain size setting can be found in Ref. [12]. The number of grid points is $500(x)\times128(r)\times112(\varphi)$, about 7.2 million in total. Figure 1(b) shows how the exit plate is attached to the nozzle.

For accurate predictions of the shear layer and the laminar sub-layer, refinements are applied to the wall boundaries to keep $Y^+ < 1$ in most of the grid and sufficient grid points that are located inside the shear layers to simulate significant velocity gradients (Fig. 2). Grid sizes are non-uniformly distributed in both the radial and axial directions. The grids are clustered near the jet exit, and the grid within the potential core of the jet is as fine as $\Delta x = 0.008d_e$. Uniform grids are used in the azimuthal direction, as Fig. 2 shows. Figure 2 also illustrates the computational domain, grid distribution, and the boundary conditions of the present two cases. The no-slip boundary condition is adopted at all the wall surfaces (surfaces of supply tube and the exit plate). At the radial boundary $R = 11.136d_e$, $p = 101325$ Pa, and $\partial u_i/\partial r = 0$ are used. At the outlet boundary ($x = 30d_e$), $p = 101325$ Pa, and the Neumann condition $\partial u_i/\partial x = 0$ (zero gradient) are taken. $p = 101325$ Pa and $\partial u_i/\partial x = 0$ are also taken at the upstream ambient boundary ($x = -5d_e$) for the case without the exit plate.

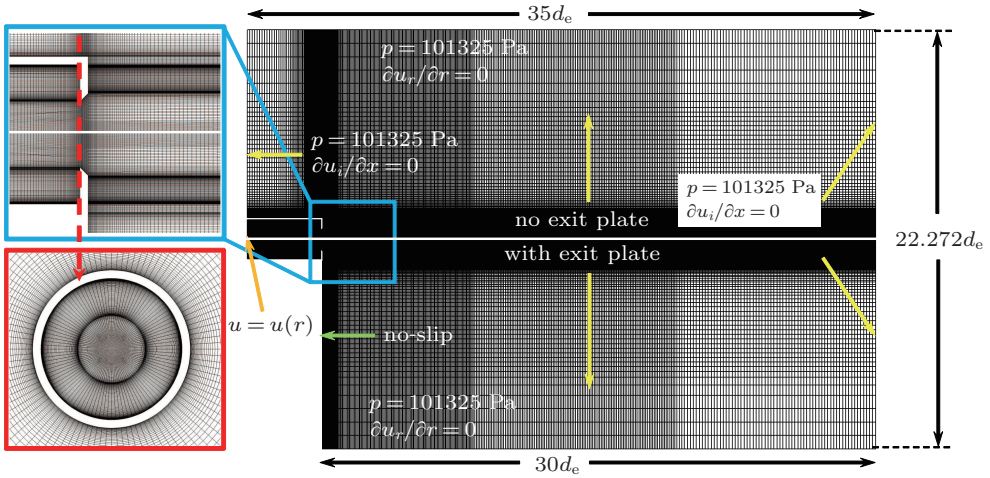

Fig. 2. (color online) Size and grid distribution of the computational domain and the boundary conditions for the present simulation (only half the computational domain of each case is shown).

Following the experiment of Mi *et al.*,[16] the inflow for the present simulations is assumed to be the fully-developed internal turbulence. Hence the velocity distribution of the inflow can be described by the empirical (1/7)-th power law, i.e.,

$$u(r) = u_{\max}\left(1 - \frac{|r|}{D/2}\right)^{1/7}, \tag{13}$$

where r is the distance from the centerline, D is the diameter of the supplying tube ('(1/7)-th inflow' is for referring this inflow condition in the following discussion). Random fluctuations are added to the inflow, and the root-mean-square (RMS) value of fluctuation amplitude is set to be $0.01u(r)$. The inflow condition is implemented using UDF in FLUENT and updated

for each time step.

The Strouhal number $S_t = fd/U_j$ (f being the frequency of occurrence of the primary vortices) of the circular jet ranges from 0.3 to 0.6 (see Ref. [28] by Gutmark and Ho). According to Mi *et al.*,[16] the Strouhal number of the jet from the orifice plate is larger than those from nozzles of the other two types. Thus, $S_t = 0.6$ is chosen in the present study so that the frequency is

$$f = \frac{S_t u_e}{d_e} = 2804 \text{ Hz}. \tag{14}$$

The time step used in the present simulations is therefore set to be Δt=2×10^{-5} s, which is fine enough to capture the occurrence of the primary vortices and their motions such as their formation and breakdown in the near-field region. The flows become stable after $1500T$, where T is a time scale defined as $T = d_e/U_j$. Flow field statistics time is $6000T$, corresponding to about 3300 primary vortices generated. The effects of grid resolution and inflow profile will also be discussed in the following section. All the computations are performed using a DELL Precision Tower T7500 with 12 CPUs.

3. Results and discussion

3.1. Characteristics of the OP jet velocity field (validation of the simulation)

Dimotakis[29] found that the influence of Reynolds number becomes insignificant in similar turbulent flows of any type when their Reynolds numbers exceed a critical value. He claimed that the critical outer-scale Reynolds number should be $Re = 1 - 2 \times 10^4$ generally for any turbulent flow. Later, Mi *et al.*[30] revealed that the normalized values of turbulent flow properties in a turbulent round jet converge asymptotically when $Re > 10^4$. Therefore, it makes sense to validate the present simulations performed at $Re = 5 \times 10^4$ by the PIV measurements of Mi *et al.*[16] in a similar jet configuration. However, with $Re = 7.5 \times 10^4$, note that the two Reynolds numbers are much larger than the likely critical value of 10^4 and thus these two OP jets are comparable.

The instantaneous vortex field in the near-field region, the mean velocities of the exit and downstream field, the centerline velocity (U_c) and fluctuating RMS velocity, the half-width (radial distance from the centerline at which $U = 0.5U_c$) and the mean entrainment rate of the jet are chosen for this validation.

First, following Mi *et al.*'s[16] and Xu *et al.*'s work,[31,32] we use a relative coordinate system at a streamwise translation speed of $0.6U_j$ (bulk mean velocity at the exit) to present the instantaneous streamlines in the longitudinal center plane which can 'visualize' the distribution of the primary vortices over a distance of $x \approx 8d_e$ (Figs. 3(a1)–3(a3)). For comparison, the PIV results given by Mi *et al.*[16] are presented in Figs. 3(b1)–3(b3).

Figure 3 shows the contours of the vorticity of the axial plane $\varphi = 0$ in different cases. We can see that eddies visualized by the streamlines match the corresponding contours, proving the effectiveness of the visualization method proposed by Mi *et al.*[16] Figure 3 clearly demonstrates that the non-axisymmetric vortices occurring in the near-field are well captured by the simulation and these vortices are apparently similar to those from the PIV measurements. The instantaneous (relative) streamlines appear to imply that ring-like structures occur in the near field, which have been reported by both experimental and numerical studies,[7,10,12] travel downstream and then break down due to their interactions with each other and with the surrounding flow. This deduction is consistent with the three-dimensional structures of the jet shown later. Both the LES results and the PIV measurements show that the vortex rings break down from about $x/d_e = 2.5$, where the vortex cannot be explicitly paired.

Figure 4 shows the comparison between the mean velocity fields in the longitudinal center plane obtained by LES and those obtained by PIV. As expected naturally from the comparison of Fig. 3, LES predicts the mean velocity field well. Looking at the near field region in Fig. 4(a), we can see that the vena contracta is also correctly simulated by LES even it is not shown by the PIV result probably due to the resolution limit. Downstream within the potential core, i.e., the region where the mean velocity is approximately constant, the predicted and measured mean flows are overall similar, i.e., the jets mix with the surroundings and spread out continuously as x increases. However, precisely there are some differences between the predictions and measurements: after the potential core, the centerline velocity predicted decays at a slightly higher rate than the measured velocity.

To examine the effects of the grid resolution and the inflow condition, two additional no-exit-plate cases, namely, a coarse mesh case (grid number of $300(x)\times84(r)\times112(\varphi)$), with the (1/7)-th inflow condition and a coarse mesh case with a uniform inflow condition, are investigated. Figure 5 shows that the exit velocity is well predicted by the present LES with the (1/7)-th inflow condition. It is worth noting that, while the SC jet exhibits a 'top-hat' inflow velocity profile, the inflow velocity profile of the OP jet is shaped like a letter 'M'. The rescaled LES result of the fine mesh case with the (1/7)-th inflow condition is very close to the HW measurement of Mi *et al.*,[14] indicating a good accuracy of the present simulation, even on the upstream flow. Also, we can see from Fig. 5 that the use of the (1/7)-th inflow condition significantly improves the prediction of the nozzle exit mean velocity while the grid refinement has a minor effect.

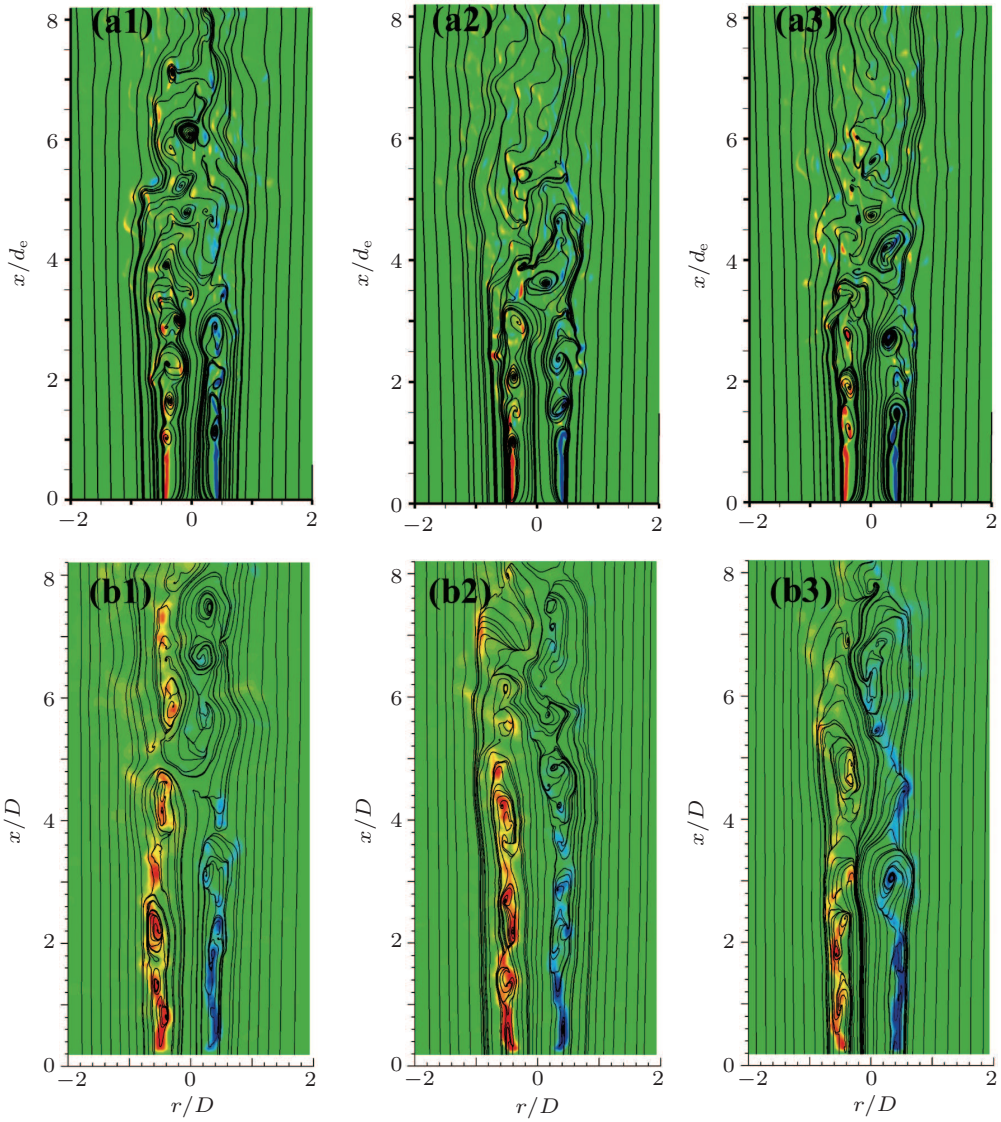

Fig. 3. (color online) Typical near-field instant streamlines, in the longitudinal center plane, under a relative coordinate system translating at $v_x = 0.6U_j$. Panels (a1)–(a3) show the LES results; panels (b1)–(b3) are the results cited from Mi *et al.*'s work.[16]

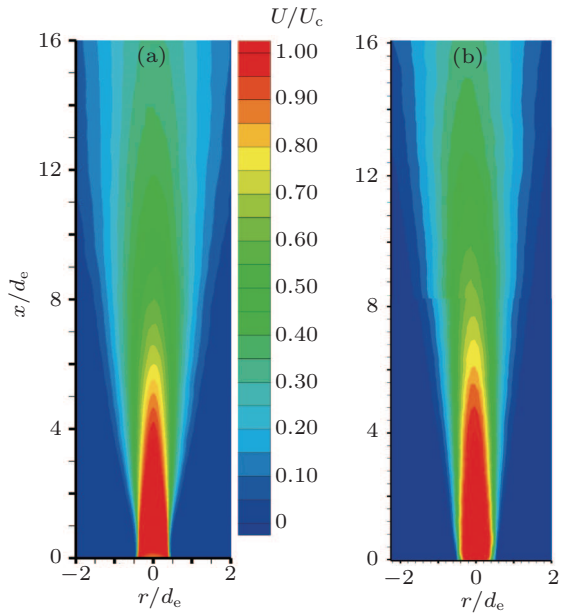

Fig. 4. (color online) Contours of the mean velocity in the longitudinal center plane, showing (a) LES result and (b) Mi *et al.*'s results.[16]

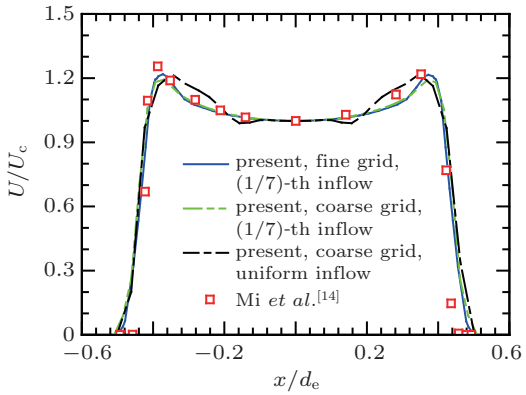

Fig. 5. (color online) Mean velocity distributions of the nozzle exit. Here U_c is the mean velocity at $x = 0.1d_e$.

Figure 6 presents the predicted centerline mean velocities of the OP jet by plotting U/U_m and U_m/U versus x/d, where U_m is the maximal mean velocity along the centerline. For comparison, the experimental results of Mi *et al.*[16] and Quinn,[15] and the predicted results of the additional cases are

also plotted in the figure. Fairly clearly, overall the predictions accord well with the measurements. Among the three simulation cases presented in Fig. 6, the fine and coarse mesh cases with the (1/7)-th inflow condition are predicted more accurately. However, the result of the coarse mesh case with uniform inflow condition displays an obvious discrepancy from the measurements. Although the difference in the result between the fine mesh case and coarse mesh case with the (1/7)-th inflow condition is minor, a fine mesh is more appropriate for simulating the three-dimensional vortical structures. Hence, the following discussion will be based on the simulations using a fine mesh and the (1/7)-th inflow condition.

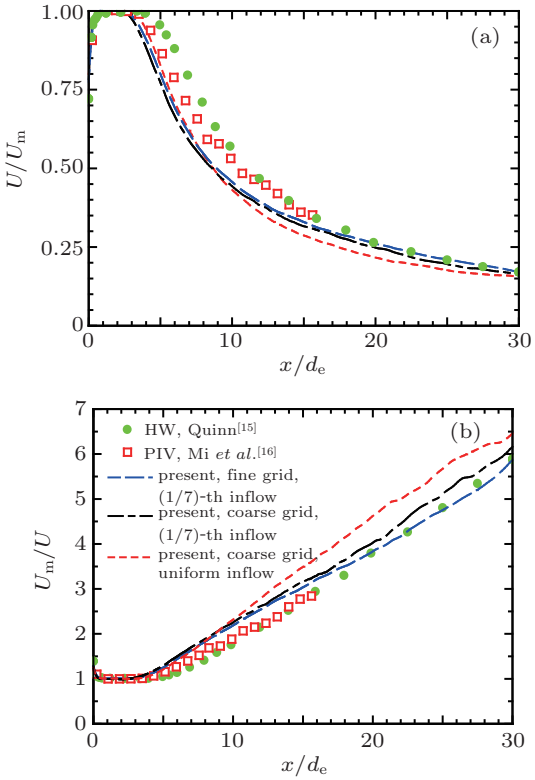

Fig. 6. (color online) Mean velocities of the centerline. (a) Normalized; (b) normalized and inversed. Here U_m is the maximal mean velocity along the centerline.

In Fig. 6, of interest, however, there is some difference occurring between $x/d_e = 5$ and $x/d_e = 20$, i.e., in the transition region, followed by a good agreement in the far field. Correspondingly, the half-width of the simulated jet is wider than that from the measurements (Fig. 7). That is, both decay rates of the centerline velocity and half-width appear to be slightly overestimated in the transition region by the present simulation. Such differences may be caused by the inflow conditions. Though we have introduced a power-law inlet velocity distribution to mimic the full developed turbulent flow in a round tube, there are other properties like Reynolds stresses of the inflow that are unknown and so cannot be considered. Also, if a careful comparison is made between the exit mean velocity distributions from the present LES prediction and the hotwire measurements[14] in Fig. 5, a small but discernible difference in the boundary layer is seen, i.e., the momentum thickness of the jet exit is predicted to be a bit thinner. According to Kim and Choi's work,[12] the jet flow is sensitive to the inflow momentum thickness: at the same Reynolds number, the thinner the inflow momentum thickness, the faster the jet decays. Considering the above reasons, the differences between the LES and experimental results in the transition region can be explained reasonably well. It is worthwhile noting that Quinn's experiment is also performed at a sufficiently high Reynolds number $Re = 1.84 \times 10^5$ so that the Reynolds number effect should be negligible when examining the discrepancy between the simulated and the experimental results according to the previous discussion.

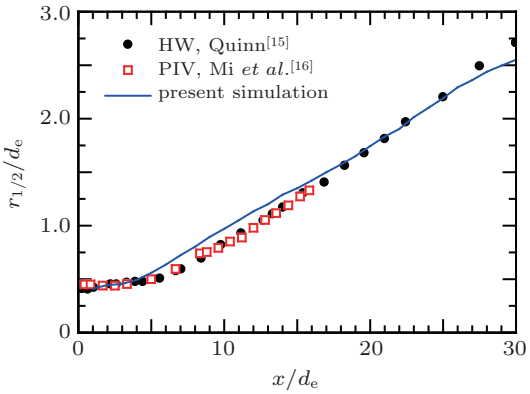

Fig. 7. (color online) Half-widths of OP jets.

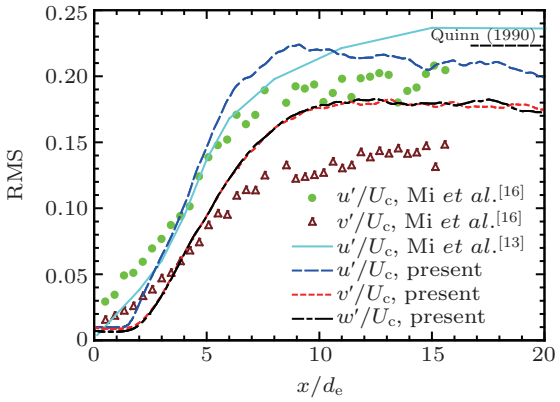

Fig. 8. (color online) RMS values of the centerline velocity fluctuations of OP jets

The centerline RMS (denoted by $u' \equiv \langle u^2 \rangle^{1/2}$, $v' \equiv \langle v^2 \rangle^{1/2}$, and $w' \equiv \langle w^2 \rangle^{1/2}$ for the three components) values of the velocity fluctuation of OP jets are presented in Fig. 8. All the three components first increase as x increases and then reach their maxima at a downstream distance and remain almost at the same level farther downstream. For any axial location, u' is larger than v' or w', and the latter two are nearly equal always. These observations are consistent with the measurements of Mi *et al.*[16] Generally, the predictions from the present simulation accord with the measurements of

Mi *et al.*[13,16] within the near-field ($x < 5d_e$) and the far-field ($x > 15d_e$). However, the present simulation overestimates the RMS values in the transition region ($5d_e < x < 15d_e$) of the OP jet, especially for v' and w'. From Fig. 8 we can see that the present simulation predicts u' quite well but the predictions of v' and w' needs improvement.

Another important property of the mixing characteristics of jet is the entrainment rate (ER). Here we propose a method to calculate the ER using the centerline velocity and half-width of the jet. ER is defined as

$$\mathrm{ER} = \frac{M - M_0}{M_0}, \tag{15}$$

where $M_0 = \rho\pi d_e^2 U_0/4$ is the inlet mass flow rate, and M is the mass flow rate of the cross section at location x, i.e.,

$$M = \int_0^\infty \rho U 2\pi r \mathrm{d}r. \tag{16}$$

Numerous previous investigations (e.g., Hussain *et al.*[2] and Mi *et al.*[16]) have suggested that in the fully developed region,

$$U = U_c\, \mathrm{e}^{-(r/r_{1/2})^2 \ln 2}, \tag{17}$$

where U_c is the centerline mean velocity. By substituting Eq. (17) into Eq. (16) and calculating the integral, we can obtain that

$$M = (\ln 2)\,\rho\pi r_{1/2}^2 U_c. \tag{18}$$

Hence,

$$\mathrm{ER} = \frac{M - M_0}{M_0} = \frac{4}{\ln 2}\left(\frac{r_{1/2}}{d_e}\right)^2 \left(\frac{U_c}{U_0}\right) - 1. \tag{19}$$

Using the data at $x/d_e \geq 8$ where the mean velocity profile approximately follows the Gaussian distribution, and linearly fitting the inversed centerline velocity and half-width of the jet, the ER can be calculated by Eq. (19).

In the fully developed region, one can derive that

$$\frac{U_m}{U_c} \propto \frac{x}{d_e}, \quad \frac{r_{1/2}}{d_e} \propto \frac{x}{d_e} \tag{20}$$

from the assumption of self-similarity. By substituting Eq. (20) into Eq. (19), we can infer that ER also has a self-similar solution in the fully developed region, i.e., the ER has a linear relationship with the normalized distance x/d_e:

$$\mathrm{ER} = \frac{M - M_0}{M_0} \propto \frac{x}{d_e}. \tag{21}$$

The ER measurements from Mi *et al.*[16] and Zaman[21] (Fig. 9) confirm Eq. (21). Note that Eq. (21) also implies the different importance of half-width spreading and velocity decay in the entrainment rate of the jet. Since ER is proportional to the square of $r_{1/2}$ but only linearly proportional to U_c, we can see that the half-width is more weighted than the centerline velocity in describing the mixing between the jet and the ambient fluid.

The good agreement between the directly-measured data and the estimated result by Eq. (19) of Mi *et al.*[16] validates the correctness of Eq. (19). Figure 9 also shows that the simulated ER accord well with the experimental results of Mi *et al.*[16] and Zaman,[21] indicating that the measured flow by Mi *et al.* can be successfully simulated by the present LES. The discrepancy between the estimated results of Quinn[15] and the present study may be due to the inlet conditions or the measurement error. The measurement of the ER usually has some uncertainties, especially in the far-field region where the hotwire signal is relatively weak. Calculation shows that 3% uncertainties in the measurements of velocity decay and half-width will cause about 9% uncertainty in the estimation of Eq. (19). Therefore, the discrepancy can be explained reasonably. In conclusion, the above comparisons suggest that the present LES can well predict the mixing characteristics, i.e., the mean profiles of the OP jet. Also, from the above RMS value comparison, we can observe some overestimations in the predicted RMS value. Therefore, the following investigations are focused mainly on the mean flow field of the OP jet.

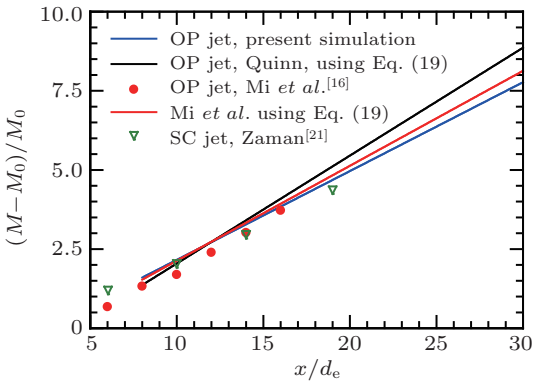

Fig. 9. (color online) Comparison between estimated and measured ERs of jets.

3.2. Effect of the exit plate on downstream mixing characteristics of the OP jet

To examine the effect of the exit plate on the evolution of the primary coherent structures, the iso-pressure surface is used to illustrate the three-dimensional coherent structures in the near-field region. Figures 10(a1)–10(a3) and 10(b1))–10(b3) show the normalized instantaneous iso-pressure surfaces at $(p - p_0)/\rho U_0^2 = -0.05$ for the cases with and without the exit plate, where p_0 is the atmosphere pressure.

Comparisons between Figs. 10(a1)–10(a3) and 10(b1)–10(b3) clearly show that the vortex ring grows and breaks at a greater axial location with the exit plate. This observation accords with the experimental results of Romano[25] using

LIF, LDA, and PTV. In his experiment, he conducted an SC water jet with 'free-slip' (the plate is placed at $2.5d_e$ behind the jet exit) and 'no-slip' (the plate is placed at the jet exit as in the case with an exit plate in the present study) boundary conditions at $Re = 6600$. The experimental configuration in Ref. [25] is quite similar to the cases in the present study, though it is not fully identical, we can make some comparisons to derive some understanding of the exit plate effect. A possible explanation for this observation is that the fluid source behind the jet is blocked by the exit plate. As the large-scale entrainment is slowed down or prevented, less Kelvin–Helmholtz instabilities may take place, which delays the formation of primary vortex rings. Another observation from Fig. 10 is that the vortex rings appear to become larger when the exit plate is attached. This observation suggests that the roll-ups last longer and thus more ambient fluid is entrained while the OP jet proceeds downstream, as the quantitative result is to be shown later in Fig. 13.

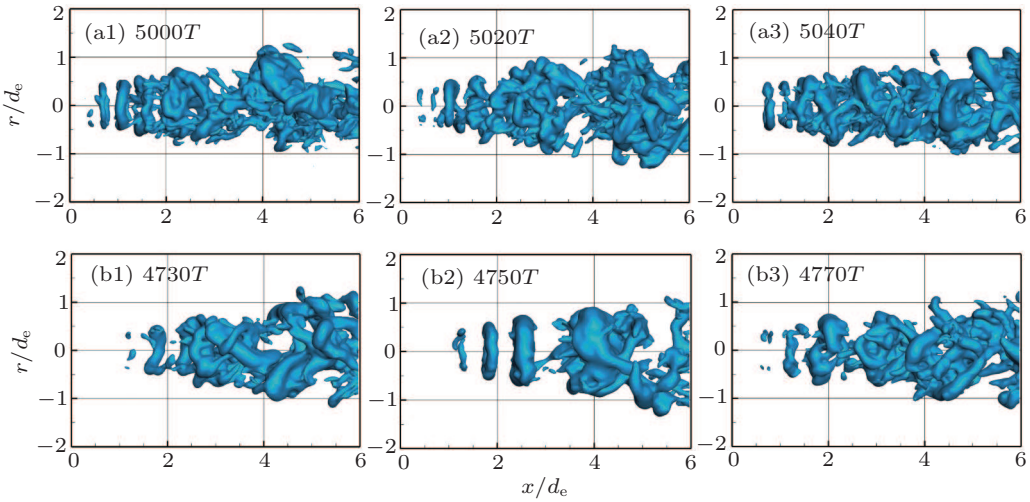

Fig. 10. (color online) Typical instantaneous iso-pressure surfaces for visualizing the vortical structures of OP jet, at ((a1)—(a3)) without exit plate and ((b1)—(b3)) with exit plate.

The previous investigations into the boundary influences on the jet mostly focused on the inner exit boundary or conditions of the nozzle which directly 'contact' the jet. By comparison, the present work concerns the influence from the outer boundary of the nozzle exit. The evolution of the vortical structures is closely related to the initial state of the jet[12,33] and so must depend on both the inner and the outer exit boundary conditions.

acteristics, the statistical results are provided. Figure 11 shows the centerline velocity decays of the OP jets. Due to the earlier breakup of the vortical structures and the increase in the number of the streamwise vortices, the velocity decays faster for the case with the exit plate. Correspondingly, the jet spreads faster as indicated by the half-widths of the OP jet in Fig. 12. These observations accord with the experimental results of Romano[25] (see Figs. 13 and 15 in Ref. [25]).

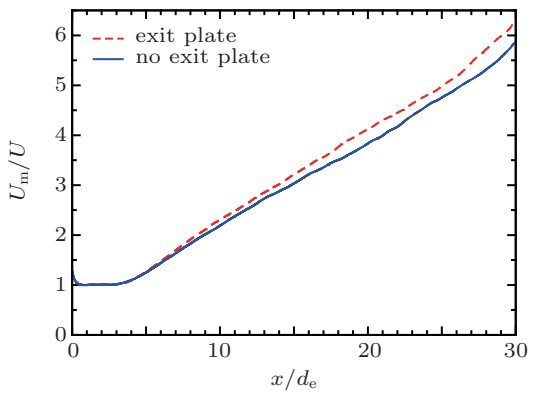

Fig. 11. (color online) Centerline velocities of the OP jet with and without an exit plate.

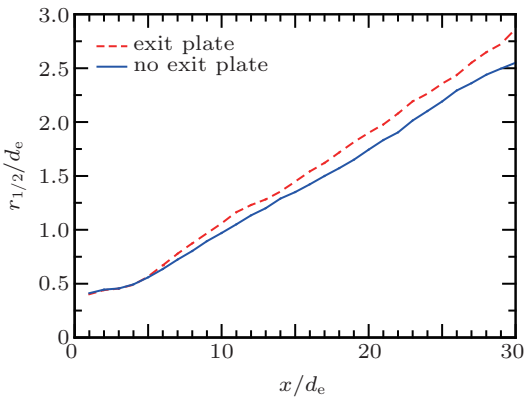

Fig. 12. (color online) Half-widths of the OP jet with and without an exit plate.

To quantify the effect of the exit plate on the mixing char-

Using Eq. (19), the entrainment rates in the two cases can

be calculated and are presented in Fig. 13. Adding the exit plate increases the entrainment rate of the present OP jet by about 10% in an axial range $8 < x/d_e < 30$, which is sufficiently larger than the likely error in computation. This is quite significant and important because it provides an idea that by controlling the upstream ambient conditions, we may enhance the mixing of the OP jet with the surrounding flow.

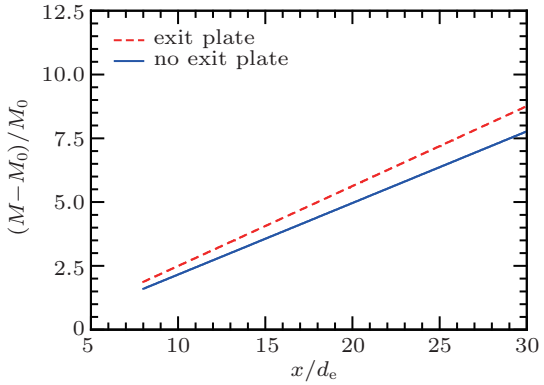

Fig. 13. (color online) Entrainment rates of the OP jet with and without an exit plate.

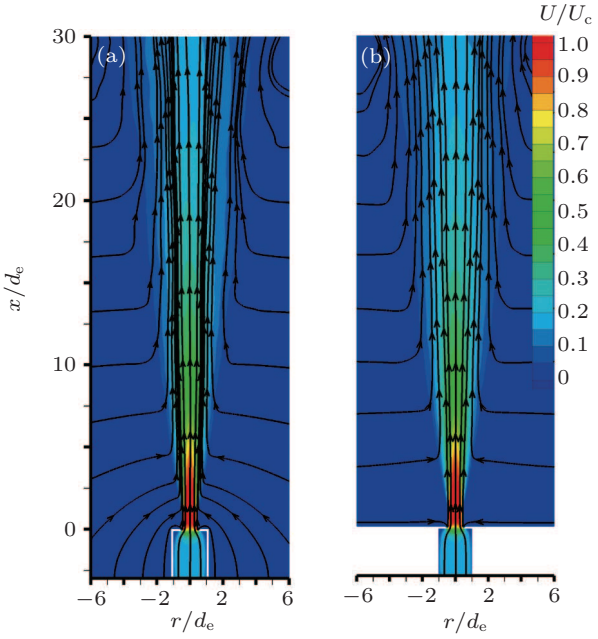

Fig. 14. (color online) Mean entrainment fields of the OP jet in the cases (a) without exit plate and (b) with exit plate.

For a more direct way of seeing how the OP jet entrains the ambient fluid, here we present the mean velocity fields of the OP jet with the mean streamlines in the longitudinal center plane in Fig. 14. The difference in how the ambient fluid is entrained for the two cases is quite obvious, particularly in the near field ($x < 5d_e$). Without the exit plate, the jet entrains ambient air from almost every direction, while the entrainment only takes place radially after placing the exit plate. The presence of the plate cuts off the fluid supply upstream from the exit plate, resulting in the later formation of the primary vortex ring with a larger size (see Fig. 10) that enhances the entrainment and mixing downstream. This also accounts for the faster decay of the centerline velocity and the wider spread of the OP jet. Note that no reverse mean flow occurs in the near field region and near the boundaries of computational domain, and the ambient fluid is entrained in the direction almost perpendicular to the axial direction.

4. Concluding remarks

In the present study, the orifice-plate (OP) jet is successfully simulated by LES. Good agreement is achieved between the present simulations and the PIV measurements of Mi *et al.*,[16] especially in mean profile. We investigate the mixing characteristics of the OP jet in the cases with and without an exit plate at a Reynolds number of $Re = 5 \times 10^4$. The investigated mixing characteristics includes instantaneous three-dimensional vortical structures, the centerline mean velocity, the half-width, and the entrainment rate of the jet. Also we propose a simple method to calculate the entrainment rate using the centerline velocity and half-width of the jet. The main conclusions drawn from the present study are as follows.

(i) In the presence of the exit plate, the centerline velocity decays faster and the jet spreads out more rapidly. This is consistent with the experimental result of Romano[25] for an SC jet. Also the entrainment rate of the present OP jet is increased by about 10% on average in an axial range $8 < x/d_e < 30$ when a cross-sectional plate is attached to the nozzle exit.

(ii) The vortical structures show significant differences for the two cases: with and without the exit plate. The plate reduces the perturbation from the ambient flow and thus the Kelvin–Helmholtz instability delays its occurring so that the primary vortex ring forms farther downstream and becomes larger, eventually the entrainment is enhanced.

(iii) The estimate by Eq. (19) of the entrainment rate using the centreline velocity and half-width of the jet is found to be approximately valid.

(iv) Both the ambient and inflow boundary conditions of an OP nozzle have significant influence on the downstream evolution of the jet.

References

[1] Wygnanski I and Fiedler H 1969 *J. Fluid Mech.* **38** 577
[2] Hussein H J, Capp S P and George W K 1994 *J. Fluid Mech.* **258** 31
[3] Hussain A K M F and Zaman K B M Q 1981 *J. Fluid Mech.* **110** 39
[4] George W K 1989 *Advances in Turbulence* (New York: Springer-Verlag) p. 39
[5] Becker H A and Massaro T A 1968 *J. Fluid Mech.* **31** 435
[6] Dimotakis P E, Miake-Lye R C and Papantoniou D A 1983 *Phys. Fluids* **26** 3185
[7] Mi J, Nobes D S and Nathan G J 2001 *J. Fluid Mech.* **432** 91
[8] Malmström T G, Kirkpatrick A T, Christensen B and Knappmiller K D 1997 *J. Fluid Mech.* **346** 363

[9] Brancher P, Chomaz J M and Huerre P 1994 *Phys. Fluids* **6** 1768
[10] Boersma B, Brethouwer G and Nieuwstadt F 1998 *Phys. Fluids* **10** 889
[11] Bogey C and Bailly C 2006 *Phys. Fluids* **18** 065101
[12] KimJ and Choi H 2009 *J. Fluid Mech.* **620** 383
[13] Mi J, Nobes D S and Nathan G J 2000 *Expt. Fluids* **28** 93
[14] Mi J, Nathan G J and Nobes D S 2001 *J. Fluids Eng.* **123** 878
[15] Quinn W 2006 *Eur. J. Mech. B: Fluid* **5** 279
[16] Mi J, Kalt P, Nathan G J and Wong C Y 2007 *Expt. Fluids* **42** 625
[17] Zaman K B M Q 1996 *J. Fluid Mech.* **36** 1
[18] Hussain A K M F 1986 *J. Fluid Mech.* **173** 303
[19] Grinstein F F and DeVore C R 1996 *Phys. Fluids* **8** 1237
[20] Stanley S A, Sarkar S and Mellado J P 2002 *J. Fluid Mech.* **450** 377
[21] Zaman K B M Q 1999 *J. Fluid Mech.* **383** 197
[22] Antonia R A and Zhao Q 2001 *Expt. Fluids* **31** 319
[23] Burattini P, Antonia R A, Rajagopalan S and Stephens M 2004 *Expt. Fluids* **37** 56
[24] Babu P C and Mahesh K 2004 *Phys. Fluids* **16** 3699
[25] Romano G P 2002 *Expt. Fluids* **33** 323
[26] Germano M, Piomelli U, Moin P and Cabot W H 1991 *Phys. Fluids A: Fluid Dyn.* **3** 1760
[27] Lilly D K 1992 *Phys. Fluids A: Fluid Dyn.* **4** 633
[28] Gutmark E and Ho C M 1983 *Phys. Fluids* **26** 2932
[29] Dimotakis P E 2000 *J. Fluid Mech.* **409** 69
[30] Mi J, Xu M and Zhou T 2013 *Phys. Fluids* **25** 075101
[31] Xu M Y, Zhang J P, Mi J C, Nathan G J and Kalt P A M 2013 *Sci. China: Phys. Mech. Astron.* **56** 1176
[32] Xu M Y, Zhang J P, Mi J C, Nathan G J and Kalt P A M 2013 *Chin. Phys. B* **22** 034701
[33] Hussain A K M F and Zedan M F 1978 *Phys. Fluids* **21** 1100